Microstructural, Mechanical, and Electrochemical Corrosion Properties of Extrusion Additive Manufactured 17-4 PH Stainless Steel

YanHan LIEW,*[a] Aloysius TAN [a] and Mojtaba SALEHI [a]

The 17-4 precipitation hardenable (PH) stainless steel is a material of choice for various applications. Near-net-shape processes, such as the extrusion-based additive manufacturing (EAM), are attractive fabrication methods due to its simplicity, safety, and cost-effectiveness. The present study aimed to conduct a systematic comparative study into microstructural, mechanical, and electrochemical corrosion performance of EAM 17-4 PH stainless steel samples across various states: as-printed, as-sintered, and post-processed. The as-sintered samples were further characterized, along and perpendicular to their build direction, including optical and scanning electron microscopy, tensile testing, and potentiodynamic polarization tests. The results demonstrated anisotropic behaviour of as-sintered samples, dependent on build orientation. The samples printed perpendicular to the build direction demonstrated better mechanical performance, with higher ultimate tensile strength (28%) and elongation to failure (eightfold) compared to those printed along the build direction. In particular, the corrosion potential and pitting potential along the build direction (-0.108 V, 0.059 V vs SCE respectively) demonstrated better electrochemical corrosion properties, as compared to perpendicular to the build direction (-0.181 V, -0.015 V vs SCE respectively). The effect of post-processing, encompassing machining and heat treatments (H900 and H1150), were investigated and compared with those of conventionally and additively manufactured 17-4 PH stainless steel counterparts, offering a holistic understanding of the intricate interplay between processing parameters, microstructural evolution, and material properties, notably in the context of electrochemical corrosion resistance.

[a] Additive Technology Innovation, Additive Manufacturing Division, Singapore Institute of Manufacturing Technology (SIMTech), Agency for Science, Technology and Research (A*STAR), 5 Cleantech Loop #01-01, CleanTech Two Block B, Singapore 636732, Republic of Singapore.

* Corresponding Author: Dr. YanHan LIEW, liewyh@simtech.a-star.edu.sg

Introduction

Among the diverse selection of precipitation hardenable stainless steels (PH SS), the 17-4 PH SS (AISI grade 630) stands out as one of the most extensively used types, owing to their exceptional weldability, austenitic/martensitic microstructure, high tensile strength, and good corrosion resistance [1,2]. Thus, 17-4 PH SS has become a material of choice for tooling and component applications, such as end effectors and turbine shafts. However, while 17-4 PH SS has superior mechanical properties, it comes at the expense of limited formability and difficulty in machinability [3]. Therefore, near-net-shape processes, such as additive manufacturing (AM), are attractive fabrication methods for 17-4 PH SS. Furthermore, there is added preference for AM in the production of tooling components attributed to the multifaceted challenges posed by traditional manufacturing methods. These challenges include the intricate geometries of tooling components, which make them difficult to machine, the costliness associated with small-batch production, and the time-consuming nature of part replacement, which is critical for ensuring uninterrupted manufacturing processes [4].

In light of these challenges, there has been a growing interest in the additive manufacturing of 17-4 PH SS, dominated by Powder-bed Fusion (PBF) techniques, such as Laser-PBF (L-PBF) [5]. However, PBF methods are encumbered by certain issues, including high capital costs, powder recycling, and safety concerns related to powder handling, such as the risk of powder explosion or inhalation [4]. Therefore, the extrusion-based AM approach has garnered attention as a potential avenue for the fabrication of metal components via a straightforward and office-friendly process of extruding metal-containing feedstock with minimal material wastage [6] and possible reduction in energy consumption [7]. Extrusion additive manufacturing (EAM) presents a pathway to exploit the advantages of efficient feedstock handling and economical material consumption for cost-effective metal part printing [8,9]. EAM, also known as Fused Filament Fabrication (FFF) or Fused Deposition Modeling (FDM), is particularly characterized by its utilization of extruded material from various formats, encompassing filaments, rods, and pellets. The recent review by Drummond *et al.* [6] provides an extensive collection of process parameters with corresponding material properties for EAM of high melting iron alloys, including 17-4 PH SS.

Researchers have explored the development of EAM for 17-4 PH SS, focusing on binder and feedstock formulation, optimization of printing and sintering parameters, and the characterization of microstructural features, mechanical properties, shrinkage, and dimensional accuracy of fabricated components. In particular, Gonzalez-Gutierrez *et al.* [10] worked on the feedstock formulation involving a proprietary binder system for 17-4 PH SS powder while Singh *et al.* [11] analyzed various sintering profiles. Pellegrini *et al*. [12] studied the distortion during sintering and geometric accuracy of the technique, followed by the influence of aging treatments on the porosity and hardness of 17–4 PH SS parts fabricated by EAM [13]. Di Pompeo *et al.* [14] and Cho *et al.* [15] explored the microstructural and mechanical aspects, while Opoz *et al.* [16] studied the effects of surface finishing and post-processing on EAM fabricated 17-4 PH SS. Although these publications have provided valuable insights into various aspects of EAM-fabricated 17-4 PH stainless steel parts, further research is necessary to advance this technology.

The primary challenges associated with parts fabricated via EAM include inferior overall properties compared to standard materials or those produced through other AM processes. These limitations are largely attributed to the presence of defects generated during fabrication and issues at the interfaces between layers and deposited materials tracks. Some of these defects are inherent nature of EAM and inevitable [17]. There is limited literature available that specifically focuses on characterizing these defects and investigating their impact on the properties of EAM-fabricated 17-4 PH SS. Recently, Mancia *et al.* [18] demonstrated that the build orientation angle significantly affects defect formation and, consequently, the tensile properties of EAM-fabricated 17-4 PH SS. Further studies are required to fully understand how these defects affect the physical, mechanical, as well as electrochemical corrosion properties of EAM-fabricated 17-4 PH SS components.

One important aspect that remains underexplored is the anisotropic nature of EAM parts relative to build orientation. This study aims to investigate the extent to which anisotropic performance in EAM-fabricated 17-4 PH SS is linked to defects. We started by characterizing the filament feedstock and the as-printed samples. The as-sintered samples were then analyzed, both along and perpendicular to the build direction, to provide a systematic comparative study of the microstructural, mechanical, and electrochemical corrosion properties of EAM 17-4 PH SS, using optical and scanning electron microscopy, tensile testing, and potentiodynamic polarization tests. Finally, the effect of post-processing—including machining and heat treatments (H900 and H1150)—was examined and benchmarked.

Methods and Materials

2.1 EAM of 17-4 PH SS Samples

Samples used in this study were printed via the Metal X™ 3D printer (Markforged, Waltham, Massachusetts, USA) and its corresponding 17-4 PH SS (UNS S17400) filament [19]. Due to the proprietary nature of its fabrication, detailed thermal history information is not available. Nevertheless, characterization and analysis of the filament was conducted in this study. Next, the prints were done using Markforged's Atomic Diffusion Additive Manufacturing (ADAM) technology, which is in essence a type of sinter-based EAM. The filament's chemical composition is, as claimed by Markforged [19], is in line with the chemical requirements for UNS S17400 type stainless steel in ASTM A564 [20].

The Metal X™ 3D printer extruded the filament layer by layer, and each layer consisted of a series of concentric walls/shells, with an infill pattern of alternating 45° angles. The printer also set a 20% increase by default from the desired geometry to accommodate the sample's shrinkage after sintering. In addition, users could opt for an additional flat build, called "raft", to have a more even thermal cooling force. Before printing, vacuum-sealed paper was placed on top of the build stage to facilitate adhesion and detachment of the 3D printed samples. The chamber and build stage were also heated throughout the printing process. Importantly, there are two main surfaces that will be compared regularly in this study (**Error! Reference source not found.**), that is the Z surface (along the build direction) and the X/Y surface (perpendicular to the build direction).

After printing, the samples were sent into the solvent-based debinding system Wash-1 (Markforged, Waltham, Massachusetts, USA), in a bath of Opteon Sion solvent for 6 hours minimum, to remove the binder. The samples were then sent for sintering in the Sinter-1 (Markforged, Waltham, Massachusetts, USA) furnace using Markforged's predetermined sintering profile. After sintering, some of the samples were subjected to further age hardening heat treatments: the H900 and H1150 standard heat treatments [20]. For each heat treatment process, the as-sintered samples were firstly solutionized at 1040°C for 1 hour (commonly referred to as Condition A [20]). The solutionized samples were then heat treated to the H900 (480°C for 1 hour) or H1150 (620°C for 4 hour) standards respectively [20].

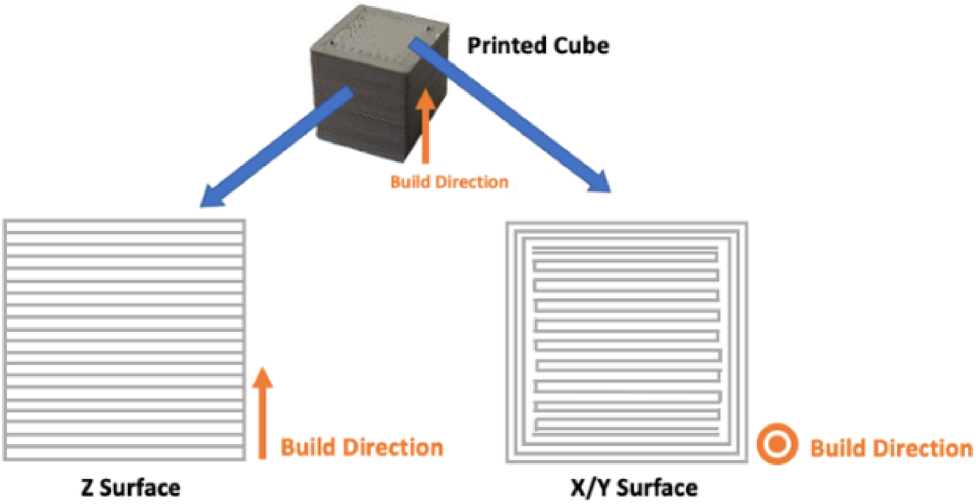

Figure 1. Schematic view of Z *surface (along the build direction)* and X/Y surface *(perpendicular to the build direction)* of an EAM printed cube.

2.2 Characterization Methods

2.2.1 Density Measurements

Two types of density measurement were used in this study: Archimedes and pycnometry. Archimedes' density measures both open and closed porosity of the structure, and was determined according to ASTM B962 [21]. On the other hand, pycnometry density measures only the closed porosity of the structure. The pycnometry density is measured using the AccuPyc II 1345 (Micromeritics Instrument Corp., Norcross, Georgia, USA), which utilizes the inert gas displacement technique to determine the apparent volume and density of the sample. The Archimedes density has a slightly lower value as compared to the pycnometer values, which could be due to the presence of open pores which are still not completely filled with water even when the samples had been immersed in water and vacuumed for 1 hour as stated in ASTM B962 [21].

2.2.2 Mechanical Tests

Tensile tests were designed according to ASTM E8 [22] for 6 mm wide subsize rectangular tensile test specimens. In order to analyze the effect of build direction on mechanical performance, vertical and horizontal tensile samples were fabricated (Figure 2a), with the build direction either perpendicular or along (collinear) the samples' build plane respectively. In general, a minimum of three replicates were conducted for each sample type; the final values reported will be the average value. The tensile specimens were pulled to failure using the Instron 5982 Universal Testing System (Instron, Norwood, Massachusetts, USA) with ±100 kN maximum loading capacity at a cross-head speed of 0.481 mm/min. This crosshead speed results in a strain rate of approximately 0.00032 s^{-1}, which lies within the prescribed range of 0.00025 s^{-1} to 0.002 s^{-1} as outlined in the ASTM E8/E8M standard. For the analysis of the surface conditions, additional tensile tests were performed on the samples printed perpendicular to the build direction; slightly larger samples were printed so that it could be machined down to the same size (**Error! Reference source not found.**a) as with the previous tests.

The hardness test was divided into two: macro- and micro-hardness. Macro-hardness test was conducted on printed cubes using Rockwell Hardness Tester (ZwickRoell Indentec, Dudley, UK) to obtain the overall hardness of the horizontal and vertical surfaces. On the other hand, microhardness test was done using MMT-X3 Vickers Micro-Hardness Tester (Matsuzawa Co., Ltd, Akita-shi, Japan) to investigate the hardness profile of the EAM sample from one edge to the opposite edge. Indentations were done from one end to the other end with a specified distance between each set of indentations. Each indentation set comprised three indentations to ensure reading accuracy. For the profile along the build direction, the spacing between successive indentation sets was maintained at approximately ± 0.7 mm. For the profile perpendicular to the build direction, the intervals within the initial and final 2 mm segments were set at approximately ± 0.35 mm, whereas the intervals for segments spanning 2 to 13 mm were approximately ± 1 mm. These deliberately established intervals were chosen to strike a balance between representing the sample's profile adequately and minimizing redundant data points. Notably, the sample surfaces were prepared by initially grinding with SiC papers and subsequently polishing using diamond suspensions to achieve a mirror-like finish prior to conducting the hardness tests.

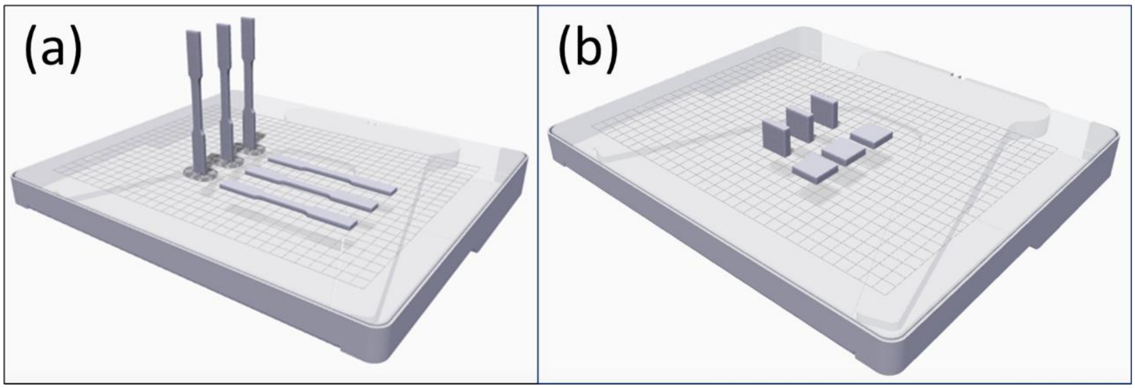

Figure 2. (a) Schematic of samples printed along (vertical) and perpendicular (horizontal) to the build direction; these samples were fabricated for the tensile tests. (b) Schematic of the 20x20x5 mm samples were fabricated for the electrochemical corrosion tests.

2.2.3 Microstructural Analysis

Optical microscopy assisted in elucidating the microstructural and porosity characteristics of the samples. The samples underwent hot mounting utilizing the CitoPress-5 Mounting Press (Struers, Ballerup, Denmark) in conjunction with PolyFast powder (Struers, Ballerup, Denmark). Then, the samples were subjected to grinding with SiC paper and polishing until achieving a reflective, mirror-like surface finish. Microstructural and localized porosity assessments were conducted using the MX51 optical microscope (Olympus, Shinjuku City, Japan). Moreover, the particle dimensions of the filament was analyzed with the Ultra Plus (Zeiss, Oberkochen, Germany) Field-Emission Scanning Electron Microscope (FE-SEM). Samples were also analyzed under the SEM with Energy Dispersive X-ray Spectroscopy (EDX) to get elemental information.

2.2.4 Electrochemical Corrosion Tests

In order to investigate the corrosion properties of EAM 17-4 PH SS, 20 mm x 20 mm x 5 mm specimens were fabricated. Similar to the tensile tests, different sets of samples, primarily distinguished by their build orientation (**Error! Reference source not found.**b) and post-printing thermal treatment, were analyzed. Furthermore, to ensure the reproducibility of the electrochemical findings, a minimum of three independent tests were conducted on three different samples within each set. Prior to electrochemical testing, the specimens were ground with SiC paper and polished to a mirror-like surface.

The electrochemical test of interest in this study mainly focuses on the potentiodynamic polarization curves; the experiments were performed using the Interface 1000 (Gamry, Warminster, Pennsylvania, USA) workstation with the standard three-electrode configuration. A saturated calomel electrode (SCE) was employed as the reference electrode, while a graphite rod served as the counter electrode. A 3.5

wt.% sodium chloride solution was utilized as the electrolyte for the electrochemical tests. To ensure the stability of the experimental setup, the open-circuit potential (OCP) of the sample was monitored for 1 hour prior to conducting the potentiodynamic polarization tests, which were performed at a scan rate of 20 mV/min in the positive potential direction, starting from -150 mV vs OCP. Unless otherwise mentioned, all potential measurements were recorded and reported with respect to the SCE reference electrode.

Results and Discussion

3.1 Characterization of the Filament and As-Printed Samples

Error! Not a valid bookmark self-reference. shows SEM micrographs of the 17-4 PH SS filament. The SS powder particles within the filament are mostly spherical and the polymeric binder holds the SS powder particles together within the filament.

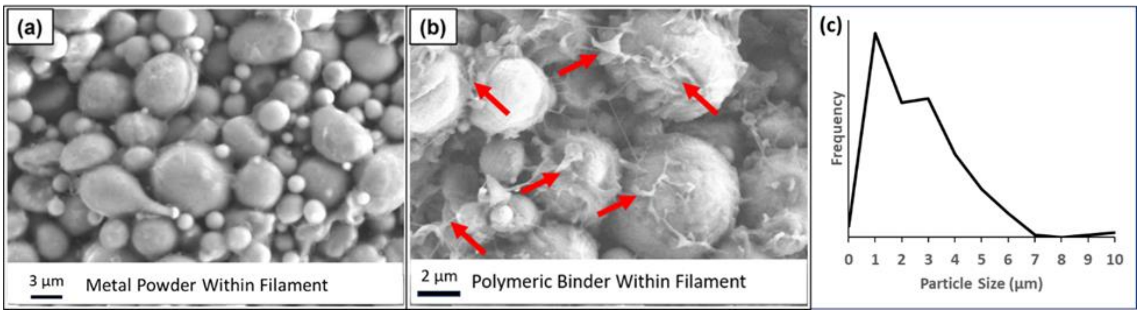

Figure 3. SEM Images of the 17-4 PH powder particles packed within the filament. Figure 3(a) illustrates the differences in morphology of the powder within the filament, while Figure 3(b) is at a higher magnification, illustrating the polymeric binder present (red arrows) within the filament. Figure 3(c) is the estimated particle size distribution of the powder within the filament, based on image analysis from 300 data points; laser diffraction was not utilized as it would require reliable separation of the powder from the other materials within the filament.

The powder particle size distribution of the 17-4 PH SS filament is obtained from analysis of SEM images, indicating particle sizes ranges from 0.62 µm to 10.65 µm with the average particle size of 3.07 µm. **Error! Reference source not found.** shows the chemical composition of the SS powder obtained from EDX analysis. As seen, the content for each element falls within the standard range, except from Cr content which is slightly above the range at 18.21 wt.%. Notably, an increased Cr content will contribute to an increased corrosion resistance of the stainless steel [23]. Furthermore, Cr is also known to be a ferrite stabilizer, and therefore austenite destabilizer in stainless steels [24].

Table 1. Chemical composition (wt.%) of 17-4 PH SS filament, according to EDX.

Sample	Cr	Ni	Cu	Mn	P	S	Nb	Si	Fe
Filament	18.21±0.05	3.37±0.16	3.68±0.30	0.32±0.01	0.01±0.01	0.02±0.03	0.02±0.01	0.39±0.01	74.01 ±0.49

Figure 4 shows SEM micrographs of as-printed 17-4 PH SS samples along and perpendicular to the build direction. The adhesion between adjacent extruded layers along the build direction was found to be insufficient and not fully bonded; this is illustrated by the red arrows and accentuated by the red dotted lines (Figure 4a). Within the center of samples perpendicular to the build direction (Figure 4b), sufficient integrity between extruded materials was observed. The higher magnification SEM micrograph in Figure 4 represents the approximate location of two extruded materials next to each other; there is no visible gap or porosity in between with virtually no micro defects. However, a clear lack of intralayer adhesion between extruded materials constituting the wall structure at the edges and corners of the samples is observed, which are generated during the printing process as gaps between adjacent extruded raster lines (Figure 4d,e). These discernible porosity gaps formed due to inadequate binding between extruded materials during the build process that needs further optimization of printing parameters, especially nozzle temperature [25]. The weaker adhesion along the build direction and at the corners and edges of samples poses a challenge to the overall density uniformity and structural integrity of the as-printed components, and in turn, sintered parts, as discussed in Section 3.2.3. One way to minimize these defects without changing the materials extrusion parameters is to alternate the orientation of successive in-fill layers that may influence layer-to-layer adhesion and, consequently, the macro-structural attributes of the printed components.

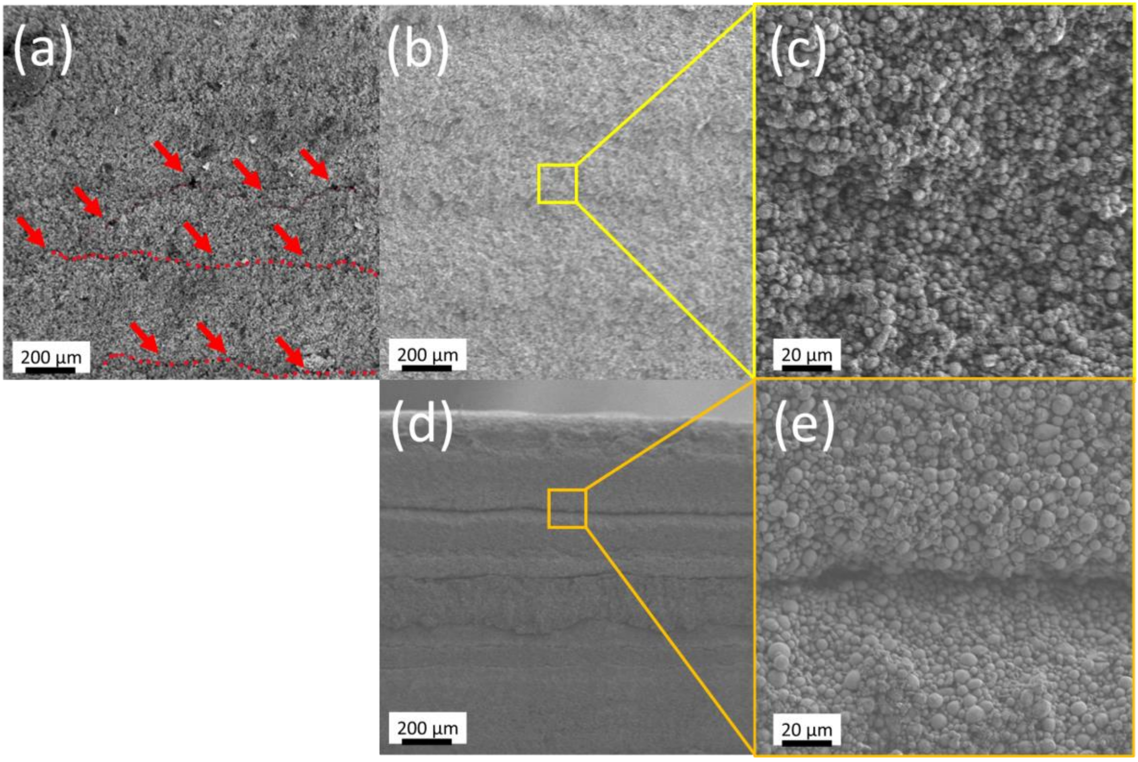

Figure 4. SEM images of as-printed green part sample (a) along the build direction, (b,c) perpendicular to the build direction at the center, and (d,e) perpendicular to the build direction near the sample edge, with magnified image shown in (d) and (e) respectively. The red arrows in Figure 4 illustrates the regions that are not fully bonded; this is highlighted by the red dotted lines.

Archimedes and gas pycnometer density of as-printed sample were determined at 4.86 g/cm^3 and 4.98 g/cm^3, respectively. This difference could be attributed to the presence of open pores in the as-printed samples, predominantly residing within the wall layers during printing (Figure 4). During the water impregnation step of the Archimedes method, water may not be able to fully penetrate within the pores/gaps even with the vacuum applied due to surface tension of the water and capillary pressure. However, Helium gas could penetrate into these gaps during density measurements by gas pycnometer, leading to a lower density measured via the Archimedes method [26]. The relative density of as-printed part based on the Archimedes method and gas pycnometer were calculated to be 62.3% and 63.8% respectively (**Error! Reference source not found.**), considering the theoretical density of the 17-4 PH SS at 7.80 g/cm^3 [27]. Overall, these density values are higher than that reported for binder jet printed 17-4 PH SS (i.e., 55-60% [28]). This higher measured density in as-printed EAM sample can be attributed to the initial close packing of the fine metal powder particles in the extruded filament, as compared to 17-4 PH SS powder lightly bounded with liquid binder during binder jetting.

3.2 Characterization of As-Sintered Samples

3.2.1 Density

During the sintering process, the sample undergoes densification through solid-state sintering, leading to the formation and growth of sinter necks between the powder particles. Subsequently, the density of the as-printed part experiences an increase post-sintering. The density values, determined using the Archimedes method (~7.42 g/cm^3), is slightly lower than those obtained via pycnometry (~7.53 g/cm^3), indicating relative densities of 95.1% and 96.5%, respectively. For extrusion-based printed 17-4 PH SS, the relative densities between of 97% and 99% have been reported after sintering in the range of 1200°C to 1360°C. [29–31]. Extrusion-based printing share similar sintering approach with other sinter-based processes such as metal injection molding and binder jetting. **Error! Reference source not found.** provides the density values reported for these technologies. In particular, as-sintered 17-4 PH SS parts manufactured using conventional MIM processes exhibit a typical density of 7.5 g/cm^3 (96.2%) [32,33]. By controlling particle size distribution, sintering atmosphere and temperature, the as-sintered density of MIM-fabricated 17-4 PH SS components can be further increased to 98.5% [34,35]. For binder jet printed and sintered 17-4 PH SS, Huber *et al.* [28] achieved relative density >99% after optimizing sintering profile. **Error! Reference source not found.** also compares these results with L-PBF, which is known for producing dense part up to 99.9% relative density [36]; LeBrun *et al.* [37] reported 98.7% density after removing surface defects while Kumar *et al.* [38] obtained 99.8% via optimizing laser energy density.

Table 2. Density of EAM parts in this study. The density values from literature, standards, and/or suppliers using similar technology are also included as reference. The theoretical density of 17-4 PH SS is taken to be that of the wrought material, at 7.80 g/cm^3.

	Density (g/cm^3)					
	EAM (This Study) Archimedes	**EAM (This Study) Pycnometry**	**MIM**	**EAM**	**BJ**	**L-PBF**
As-Printed	4.86 ± 0.01 (**62.3%**)	4.98 ± 0.01 (**63.8%**)	-	4.98 (**63.8%**) [29]	(**55 – 60%**) [28]	7.7 (**98.7%**) [37] (**98.8%**) [39] (**~99.9%**) [36] (**99.8%**) [38]
As-Sintered	7.42 ± 0.02 (**95.1%**)	7.53 ± 0.02 (**96.5%**)	7.50 (**96.2%**) [32,33] 7.58 – 7.66 (**97.2 – 98.2%**) [34] 7.58 – 7.68 (**97.3 – 98.5%**) [35]	(**96 – 96.4%**) [19,40] 7.56 (**96.9%**) [41] (**~90%**) [42] (**>99.4%**) [29] (**>97%**) [15]	7.5 – 7.66 (**96.2 – 98.2%**) [43] 7.60 – 7.65 (**97.4 – 98.1%**) [44] 7.7 (**98.7%**) [45] (**96 to >99%**) [28]	

3.2.2 Microstructure

Figure 5 presents the microstructure of the as-sintered samples, examined along and perpendicular to the build direction. Inadequate interlayer adhesion along the build direction is clearly visible, both within the center and near the edges (Figure 5a). Image analysis of the optical micrographs quantifies the average porosity as 6.5% in the central region and 6.9% near the edges, suggesting that insufficient interlayer bonding, as previously highlighted (Figure 4a), is the primary source of this defect. This defect is critical, as it directly influences the mechanical properties of the as-sintered samples (Section 3.2.3).

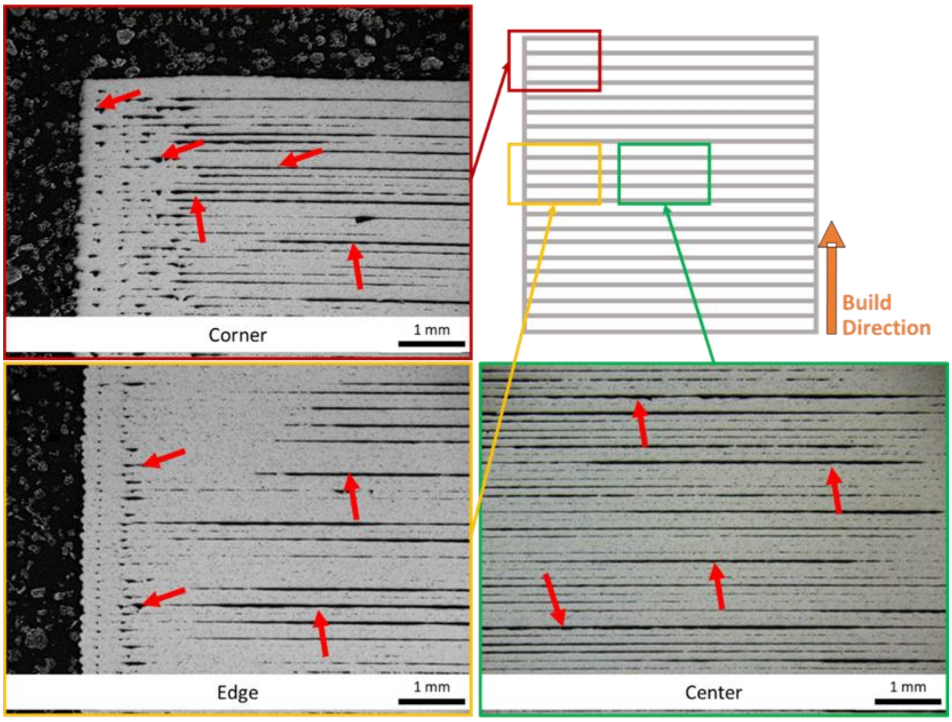

Figure 5(a). Optical microscopy of the as-sintered 17-4 PH samples (cubes) along the build direction. The orange arrow indicated the build direction, while the red, yellow, and green boxes illustrate the microstructure of the corner, edge, and center regions respectively. The red arrows points at some of the visible printing defects.

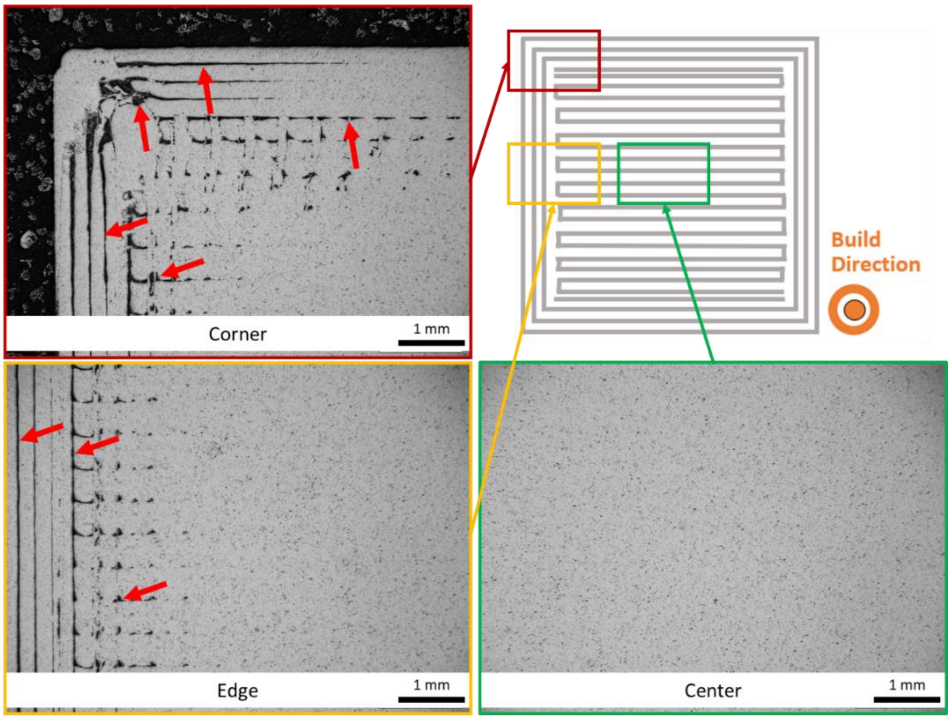

Figure 5(b). Optical microscopy of the as-sintered 17-4 PH samples (cubes) perpendicular to the build direction. The orange arrow indicated the build direction, while the red, yellow, and green boxes illustrate the microstructure of the corner, edge, and center regions respectively. The red arrows points at some of the visible printing defects. Importantly, there were no visible printing defects in the center region.

When examined perpendicular to the build direction, the as-sintered samples exhibit two distinct microstructures between the central and edge/corner regions. Within the central region, the microstructure is more consistent, with no discernible intralayer gaps (Figure 5b). The etched microstructure (using Viella Reagent for 60 seconds) within the central region reveals an equiaxed grain structure with an average grain size of 29.6 µm, based on image analysis of 300 data points. Isolated pores are present, and image analysis indicates a lower porosity of 2.6% ± 0.6%. In contrast, the microstructure near the edges and corners, as shown in Figure 5, reveals inadequate adhesion between extruded material layers, which originated from the as-printed samples (Figure 4d,e). The porosity in these areas ranges from 5.1% to 7.2%, highlighting the variability in microstructural quality across different regions of the samples.

3.2.3 Mechanical Properties

Figure 6**Error! Reference source not found.** illustrates the microhardness profiles along and perpendicular to the build direction measured across the as-sintered sample's cross-sectional surface. The average microhardness values fluctuated in the range of 82 – 364 HV along the build direction, with less pronounced fluctuations of average values 351 ± 25 HV across the middle of the profile. This fluctuation closely corresponds to the visible gaps observed in the microstructure (Figure 5a), which are attributed to printing defects rather than porosity alone. These defects, particularly near the edges and between extruded layers, result from inadequate interlayer adhesion and contribute to the localized weaknesses that cause sharp dips in microhardness. In particular, more inconsistency and flaws in the microstructure caused higher fluctuations in microhardness values, leading to anisotropic behavior in the fabricated samples based on build orientation.

Perpendicular to the build direction, there is a relatively uniform microhardness with an average value of 362 ± 15 HV across the middle of the profile, supported by the microstructural observations (Figure 5b). However, significant fluctuations in microhardness values, ranging from 66–347 HV at the start and end of the profile, are observed. These variations are similarly linked to the inadequate interlayer adhesion near the edges. The macrohardness values along and perpendicular to the build direction across the as-sintered sample's cross-sectional surface was measured to be 20 and 30 HRC respectively. These values fall within the range of MIM standards [32,33] and EAM [46], while it is slightly lower that the values for the wrought condition [27].

Figure 7 illustrates the representative tensile stress-strain curves for the as-sintered samples obtained along and perpendicular to the build direction. The corresponding values for ultimate tensile strength (σ_{UTS}), yield strength (σ_y), and elongation to failure (ε_f) are listed in **Error! Reference source not found.**. The samples printed perpendicular to the build direction exhibited greater mechanical performance in the σ_{UTS} (28%) and σ_y (~4%), as compared to the samples printed along the build direction. The mechanical property results further indicated the anisotropic behavior of 17-4 PH SS fabricated by EAM in different build orientation. In particular, the ε_f for the samples printed along the build direction compared to the perpendicular direction was reduced to 0.4% from 3.6%. This brittle fracture of the sample is due to the presence of layering defects between the filament raster line/path (Figure 5). The crack initiated and propagated along these defects, as seen from the inset images in Figure 7. Additionally, these defects act as stress concentration points leading to premature failure during the tensile test. The effects of build orientation on anisotropic behavior of EAM fabricated materials has been reported [30,31].

Amidst various influencing factors, porosity is one of the paramount determinants of the mechanical characteristics of materials [47]. The relationship between strength and porosity is fundamentally inverse, owing to the fact that structural pores not only diminish the load-bearing surface but also function as focal points for stress concentration and subsequent cracking. The following is a simple model of strength versus relative density generally applied in powder metallurgy [47]:

$$\sigma = \sigma_S\left(\frac{\rho}{\rho_S}\right)^M \tag{1}$$

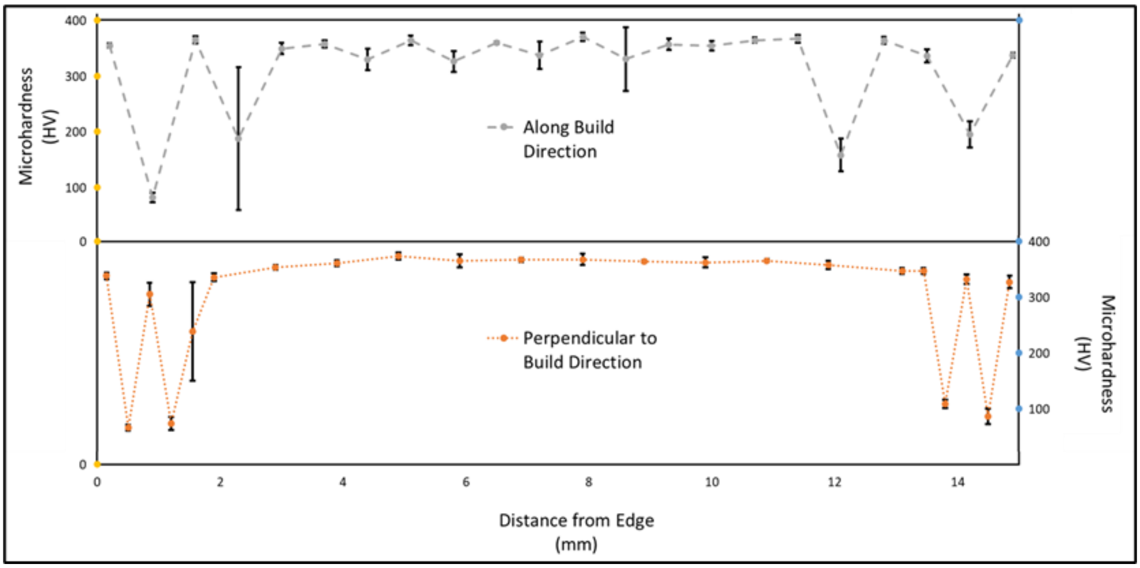

Figure 6. Microhardness profile of the as-sintered EAM 17-4 PH SS samples (cubes), (top) along and (bottom) perpendicular to the build direction.

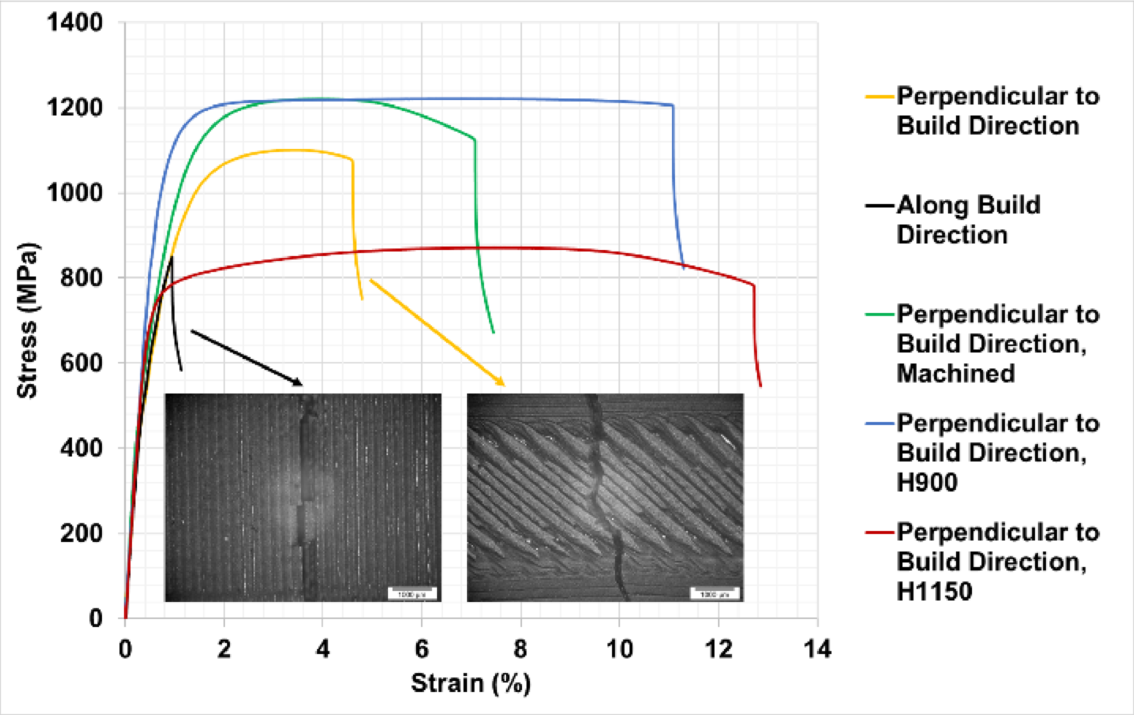

Figure 7. Representative stress-strain curves obtained in this study.

Table 3. Mechanical properties of the as-sintered EAM 17-4 PH parts. The typical values from literature, standards, and/or suppliers using similar technology are also included as reference.

	Ultimate Tensile Strength (MPa)	**0.2% Yield Strength (MPa)**	**Elongation to Failure (%)**	**Macrohardness (HRC)**
Along the Build Direction (This Study)	846 ± 6	725 ± 25	0.4 ± 0.1	20 ± 1.1
Perpendicular to the Build Direction (This Study)	1085 ± 23	753 ± 44	3.6 ± 0.3	30 ± 0.3
Perpendicular to the Build Direction, Machined. (This Study)	1219 ± 4	704 ± 49	5.9 ± 0.6	-
MIM	790 – 900 [32,33]	650 – 730 [32,33]	4 – 6 [32,33]	27 [32,33]
EAM	776 [46]	604 [46]	6.7 [46]	24.7 – 27.2 [46]
BJ	1050 [28]	-	4.1 [28]	24 ± 1 [44]
L-PBF	1357.9, 1423.6 [48] 940, 1060 [49] 1050 [50] 1180 [38] 1156 [51]	576.6, 527.1 [48] 580, 650 [49] 650 [50] 881 [51]	18.2, 15.3 [48] 5.8, 14.5 [49] 9.7 [50] 45 [38] 32.7 [51]	-
Wrought, Condition A.	1103 [27]	1000 [27]	5 [27]	35 [27]

Here, σ denotes the strength of a porous material, σ_S represents the strength of a fully dense material, ρ is the density of the porous material, ρ_S is the density of a fully dense material, and M stands for a proportionality constant, such as 2.5-6 for alumina [47] and approximately 6 for Ti [52], and 3.53 for Mg [53].

As previously discussed, the average porosity within the central region of the sample along and perpendicular to the build direction is 2.6% and 6.5% respectively. Considering these values and the σ_{UTS} values for the as-sintered samples along and perpendicular to the build direction (**Error! Reference source not found.**), the following equation can be formulated:

$$\sigma_A = \sigma_P (\frac{\rho_A}{\rho_P})^M \tag{2}$$

where σ_A is the σ_{UTS} for samples printed along the build direction, σ_P is the σ_{UTS} for samples printed perpendicular to the build direction, ρ_A is the average density within the central region for samples printed along the build direction, ρ_P is the average density within the central region for samples printed perpendicular to the build direction, and M is a proportionality constant. Using Equation 2, the value of M was determined to be 6.1, indicating that the strength of the as-sintered sample is directly proportional to its relative density raised to the power of 6.1. This result highlights a pronounced dependency of tensile strength on porosity in structures fabricated through EAM.

3.2.4 Electrochemical Corrosion Properties

Error! Reference source not found. illustrates the representative potentiodynamic curves measured in 3.5 wt.% NaCl solution for the two different build orientations in this study. Table 4 presents the corresponding corrosion potential (E_{Corr}) and pitting potential (E_{Pit}) results, together with those reported in relevant literature [54–58] with similar experimental conditions. There exist noticeable differences in the electrochemical behavior between the two build orientation. The E_{corr} along the build direction (-0.108 ± 0.008 V) was found to be more noble compared to the perpendicular direction (-

0.181 ± 0.013 V). Similarly, the E_{pit} along and perpendicular the build direction was determined to be 0.059 ± 0.010 V and -0.015 ± 0.006 V respectively. Interestingly, these results indicate that as-sintered samples along the build direction is more resistant to both localised and non-localised corrosion. While Equivalent weight (Q) and corrosion rates in mpy or mmpy are commonly used to assess general non-localised corrosion behavior and are related to parameters such as i_{Corr} and E_{Corr}, the focus in this study is on the localized corrosion mechanisms, particularly through the examination of pitting potential; localized breakdown is dangerous because it can cause rapid, concentrated material loss, lead to unexpected structural failures, and significantly compromise safety and performance, often going undetected until severe damage occurs.

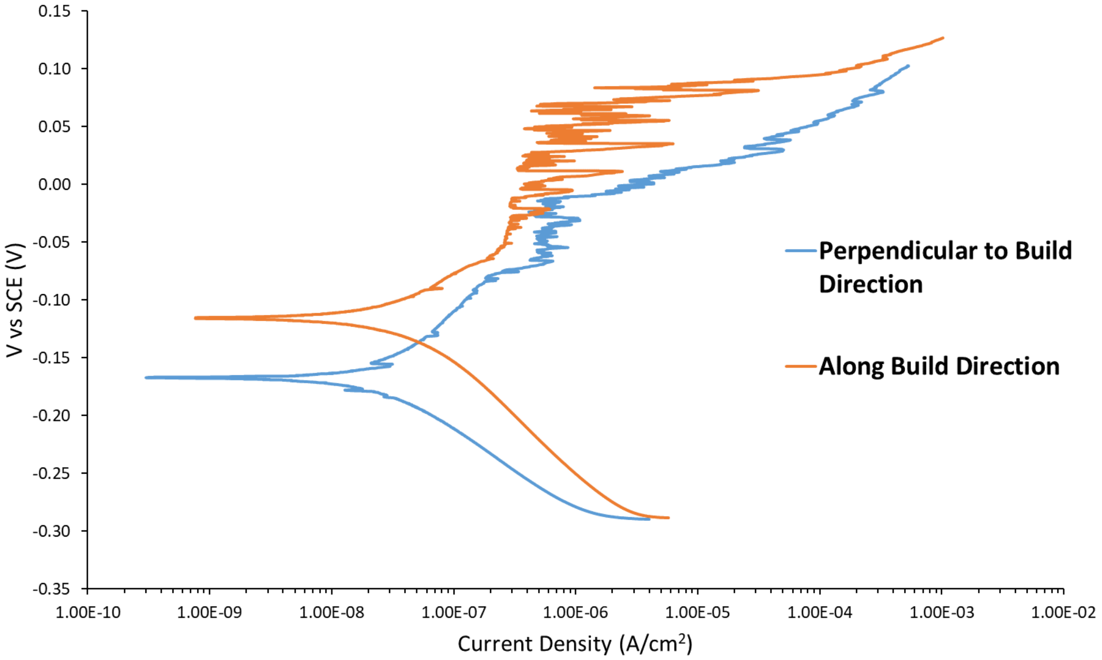

Figure 8. The representative potentiodynamic polarization curves measured on the cross-sectional surface along and perpendicular to the build direction of as-sintered 17-4 PH SS specimens.

Pitting corrosion, a localized and destructive form of corrosion, is common and predominant in stainless steel [23]. In this form of corrosion, the dissolution of the oxide layer occurs locally, leading to the formation of pits, which can propagate rapidly, eventually resulting in the failure of the material [23]. The initiation of pitting corrosion in stainless steel has been attributed to the presence of specific precipitates or segregation of elements [23,59], which are a result of the inhomogeneity of the alloy microstructure. Once initiated, pitting corrosion can continue to propagate if the localized conditions in and around the pits can sustain and promote the corrosion process, such as a decrease in pH or the presence of aggressive ions [23].

It is well known that porosity and pore defects can act as preferential sites for localized pitting/crevice corrosion to occur [54,60]. Accordingly, it would be anticipated that the as-sintered samples along the build direction, with larger line defects and more porosity (Figure 5), would have more preferential sites for localized corrosion to propagate. Surprisingly, the obtained results demonstrated that the as-sintered samples along the build direction had superior corrosion performance, when compared to perpendicular to the build direction. In other words, the presence of the defects along the build direction had instead enhanced its corrosion resistance. Similarly, in EAM fabricated 17-4 PH SS, Forcellese *et al.* [55] have shown from their potentiodynamic curves that the sintered specimens along the build direction exhibited better general corrosion resistance properties (more noble E_{corr})

compared to specimens perpendicular to the build direction. However, the root cause for this observation was not discussed by the authors.

Table 4. Comparison of the E_{Pit} and E_{Corr} results obtained with those in similar literature.

	E_{Corr} (V vs. SCE)	E_{Pit} (V vs. SCE)
Perpendicular to Build Direction (This Study)	-0.181 ± 0.013	-0.015 ± 0.006
Along Build Direction (This Study)	-0.108 ± 0.008	0.059 ± 0.010
Perpendicular to Build Direction, H900 (This Study)	-0.206 ± 0.019	0.107 ± 0.004
Perpendicular to Build Direction, H1150 (This Study)	-0.178 ± 0.031	0.165 ± 0.016
Wrought	-0.192 [54]	0.028 [54]
Wrought, H900	-0.120 to -0.130 [57]	0.173 [57]
Wrought, H1150		0.124 [57]
MIM	Approx. -0.600 [58]	Not Distinguishable [56]
EAM	-0.124, -0.126, -0.137 [55]	Not Distinguishable [55]
L-PBF	-0.293 [54]	Not Distinguishable [54]

Given the microstructural differences between the two build orientations (Section 3.2.2), we hypothesize that the large defects for the samples along the build direction could have established a different local electrochemical environment when exposed to the electrolyte and its aggressive ions and hinder the flow of ionic species locally. This hypothesis is supported by the distinctive fluctuations below the E_{pit} observed for the two build orientations (Figure 8), whereby there are transient increases in anodic current density before returning to the passive current density. This suggests the formation of metastable pitting that were unable to sustain propagation and experienced rapid repassivation, resulting in pit growth arrest [61]. The abundance of metastable pits observed in the present study exceeds those reported for a conventional wrought 17-4 PH SS [54], implying that many, if not most, of these pits may have nucleated from the defects present.

In comparing the shape of the potentiodynamic polarization curves with literature, the curves for the MIM specimens [56], EAM specimens [55] (after 30 mins of OCP), and the L-PBF specimens [54] (after 1 hour of OCP) showed no typical passive region and no characteristic rapid increase of the anodic current density below the oxygen evolution potential; this was labelled as "Not Distinguishable" in Table 4. Usually, the lack of a typical passive region would indicate that the specimen is exhibiting an "active metal" behavior whereby the oxide film on the specimen (metal) is unstable and not protective [61]; in such cases, the E_{pit} can be said to coincide with the E_{Corr}. The polarization curves obtained in this study (Figure 8) exhibited a fairly typical passive region for both build orientations. In terms of E_{corr}, the obtained results are in similar ranges (Table 4) with that of the wrought 17-4 PH [54] and EAM 17-4 PH [55] in similar experimental conditions. The E_{corr} results (-0.108 V & -0.181 V) obtained in this study are more noble than that of as-sintered MIM specimens (approximately -0.600 V) by Kazior [56] and L-PBF specimens (-0.293 V) by Schaller *et al.* [54]. Overall, these findings suggest that sinter-based AM fabricated components may possess electrochemical characteristics that differ from those of conventionally produced wrought parts. Importantly, it should be re-iterated that the corrosion characteristics of sinter-based AM parts will likely also deviate from those of L-PBF AM parts [54,62], which involves rapid heating and cooling (resulting in non-equilibrium phase formation).

3.3 Characterization of Post-Processed Samples

3.3.1 Influence of Surface Condition on Mechanical Properties

Based on the previous analysis, the samples printed perpendicular to the build direction exhibited greater mechanical properties as compared to the samples printed along the build direction. Hence the focus for this section is on the samples printed perpendicular to the build direction. The extent of structural strength is compromised by the presence of defects, especially surface defects. Microstructural characterization (Figure 5b) indicated that there were more defects on the surface of the as-sintered sample as compared to its central region. Therefore, we conducted machining process to remove those surface defects by milling 2 mm material removal from each surface of the as-printed tensile specimen. As seen in Figure 7 and **Error! Reference source not found.**, the machined sample showed an improvement from 1085 MPa to 1219 MPa in its σ_{UTS} (12% improvement), and 3.6% to 5.9% in its ε_f (63% improvement). Essentially, the machining process had removed all surface defects (i.e., 5.1% to 7.2% porosity in Figure 5b). This is in line with the inverse relationship between strength and porosity that was previously discussed in Section 3.2.3. Additionally, ductility was improved as there are lesser surface imperfections that could act as stress concentrators. Overall, this comparison demonstrated that while the wall layers provide structural shape for the printing process, parallel laying of raster lines led to lower mechanical strength as compared to cross layer perpendicular overlaps. This serves as a design consideration when determining the part slicing and rastering strategy, to minimize or eliminate the defects in the as-printed part.

Overall, the results obtained in this study further indicated that the EAM 17-4 PH SS can provide comparable, or even superior, mechanical properties, compared to the other similar or conventional sinter-based technologies (**Error! Reference source not found.**). In comparing with other fabrication methods for 17-4 PH SS, the σ_{UTS}, σ_y and ε_f of the machined samples is superior to BJ [28], other EAM [46], and the standards in MIM [32,33]. When compared to the typical wrought 17-4 PH SS, the σ_{UTS} and ε_f are greater, but the σ_y is inferior. Meanwhile, the machined EAM parts in this study can also obtain comparable σ_{UTS} to the L-PBF fabricated samples. In general, L-PBF 17-4 PH SS parts in literature [38,48–51] have displayed much higher ε_f. This is likely due to the L-PBF parts having less porosity and more refined grain size [36] as compared to the EAM fabricated parts (Section 3.2.2).

3.3.2 Influence of Heat Treatments on Mechanical and Electrochemical Corrosion Properties

The samples printed perpendicular to the build direction also undergone heat treatments to produce type H1150 and H900 specimens. The H900 heat treatment typically results in higher strength and hardness for the 17-4 PH SS, while the H1150 provides a better balance between (lower) strength and (higher) toughness. As seen in Figure 7 and Table 5, the H900 sample showed an improvement in its σ_{UTS} (14%), σ_y (41%), ε_f (125%), and macrohardness (27%). Meanwhile, for the H1150 sample, there was an improvement in ε_f (203%), at the expense of a reduction in σ_{UTS} (19%). The average area under the stress-strain curves for as-sintered, H900, and H1150 samples were calculated to be 41.8, 104.1, and 94.7 MJ/m^3 respectively. Overall, both heat treatments resulted in an improvement in the material toughness. The enhanced strength observed in H900 samples can be attributed to precipitation strengthening facilitated by copper precipitates, a phenomenon extensively documented in various studies [21,37,63]. Conversely, the heightened ductility seen in H1150 samples is attributable to the presence of retained austenite and the coarsening of copper precipitates. X-ray diffraction (XRD) analysis, as shown in **Error! Reference source not found.**, revealed the formation of retained austenite in the H1150 samples, with distinct austenite peaks indicating its presence. The retained austenite contributes to the mechanical softening observed in these samples. In contrast, the as-sintered and H900 samples primarily exhibit body-centered cubic (BCC) peaks, which are characteristic of a martensitic matrix. The XRD analysis of these samples confirms a predominantly martensitic structure. This phase transformation, as detected by XRD, provides insights into the structural changes that enhance the ductility of the H1150 samples and elucidates the role of phase composition in the observed mechanical properties.

Table 5. Mechanical Properties of Heat Treated H900 & H1150 EAM 17-4 PH SS in this study. The typical values from literature, standards, and/or suppliers using similar technology are also included as reference.

	Ultimate Tensile Strength (MPa)	**0.2% Yield Strength (MPa)**	**Elongation to Failure (%)**	**Macrohardness (HRC)**
Perpendicular to the Build Direction (This Study)	1085 ± 23	753 ± 44	3.6 ± 0.3	30 ± 0.3
Perpendicular to the Build Direction, H900. (This Study)	1235 ± 17	1063 ± 4	8.1 ± 1.6	38 ± 0.8
Perpendicular to the Build Direction, H1150. (This Study)	875 ± 6	726 ± 20	10.9 ± 1.5	30 ± 0.6
MIM, H900	1070 – 1190 [32,33]	965 – 1090 [32,33]	4 – 6 [32,33]	33 [32,33]
BJ, H900	912 ± 35 [43] 1070 – 1310 [64] 900 ± 20 [45] 1294 ± 11 [65]	660 ± 40 [43] 970 – 1030 [64] 655 ± 26 [45] 1079 ± 88 [65]	5.9 ± 2 [43] 4 – 12 [64] 10.9 ± 0.9 [45] 5.65 ± 0.4 [65]	26.4 ± 1 [43] 35 – 41 [64] 29.5 ± 1.5 [45] 39 ± 1 [44]
BJ, H1150	1001 ± 29 [65]	760 ± 71 [65]	3.18 ± 0.3 [65]	-
L-PBF, H900	~960, 1240 [50] 1417 ± 6 [37] 1390 [51]	~725, ~925 [50] 945 ± 12 [37] 897 [51]	~3.5, ~4.3 [50] 11.7 ± 0.8 [37] 29.9 [51]	-
L-PBF, H1150	1319 ± 2 [37]	1005 ± 15 [37]	4.8 [37]	-
Wrought, H900. ASTM A564	1310 [20]	1170 [20]	10 [20]	40 [20]
Wrought, H1150. ASTM A564	930 [20]	725 [20]	16 [20]	28 [20]

Overall, the results serve as a good indicator and benchmark of the mechanical properties of the typical EAM heat treated H900 and H1150 samples. In comparing with other fabrication methods for heat treated 17-4 PH SS, the heat treated H900 and H1150 samples had comparable mechanical properties to BJ [65] and the standards in MIM [32,33], while these values are inferior to the typical wrought [20] and L-PBF [37] counterparts.

Figure 10 shows the representative potentiodynamic polarization curves for the H900 and H1150 heat-treated samples together with the as-sintered sample, while Table 4 presents the E_{Corr} and E_{Pit} values. Overall, the E_{Corr} values of the H900 (-0.206 ± 0.019 V) and H1150 (-0.178 ± 0.031 V) specimens are in similar range with that of the as-sintered sample (-0.181 ± 0.01 V). Furthermore, the E_{Pit} values of the H900 (0.107 ± 0.004 V) and H1150 (0.165 ± 0.016 V) specimens are much nobler than that of the as-sintered sample (-0.015 ± 0.01 V); the heat treatments significantly improved the pitting corrosion resistance of the EAM fabricated 17-4 PH SS.

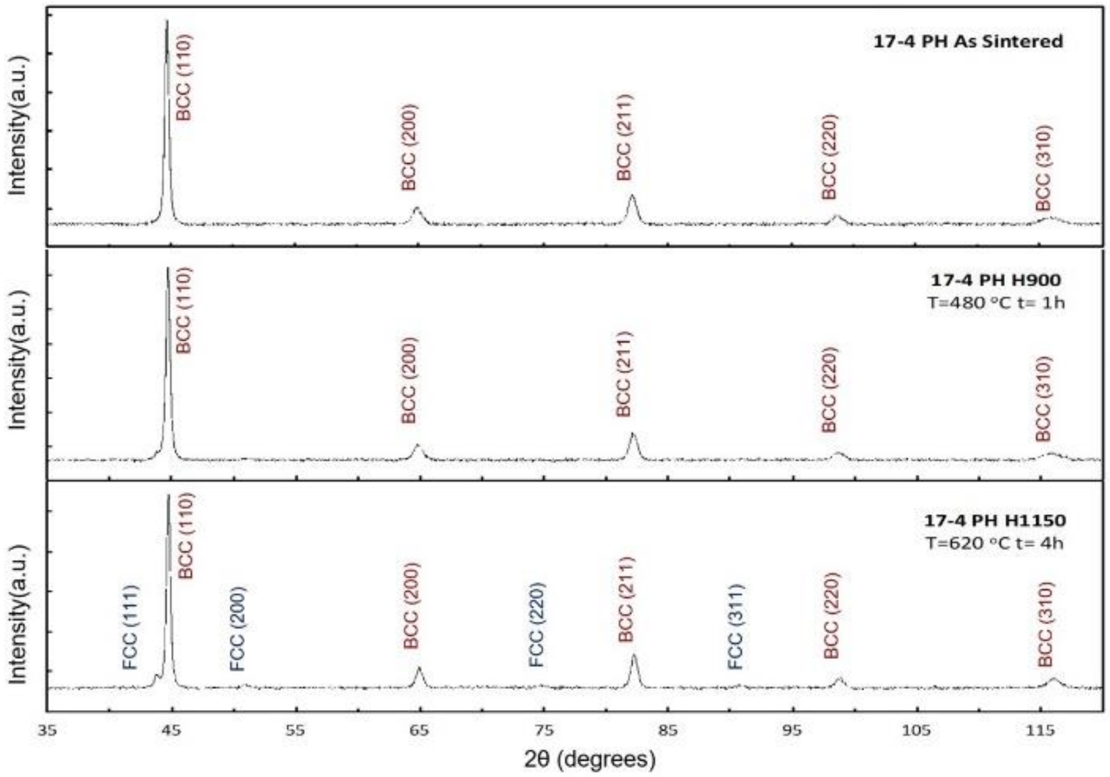

Figure 9. XRD peaks of as-sintered, H900, and H1150 EAM 17-4 PH SS in this study. The FCC peaks implies retained austenite.

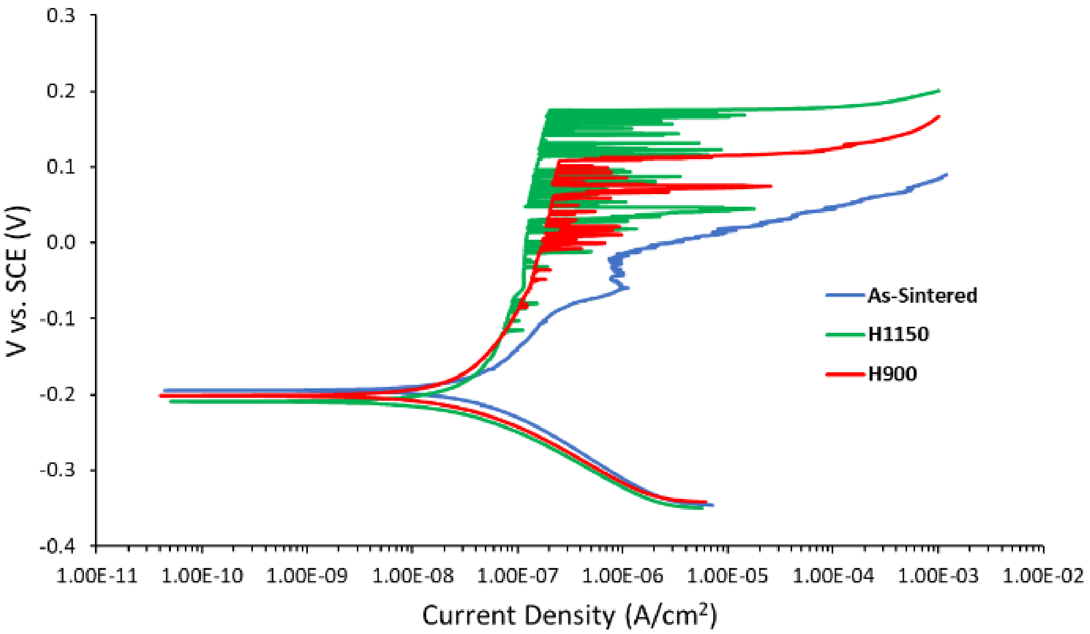

Figure 10. Comparison of the representative potentiodynamic polarization curves for the samples perpendicular to the build direction as-sintered, and after going through heat treatments.

In comparing the electrochemical corrosion properties obtained here with the literature, the E_{Corr} values for the heat treated samples were more active when compared to the approximate -0.120 V to -0.130 V range of wrought H900 and H1150 [57]. The potentiodynamic polarization curves indicated that the H1150 samples had the better pitting corrosion resistance, as compared to the H900 samples. Overall, there has been a general consensus in literature suggesting that H900 parts should be achieving improved localised corrosion resistance compared to H1150 parts, which is in contradiction with the results seen in this study. Shoushtari [57] showed that when increasing the heat treatment temperature and duration from H900 (480°C, 1 hour) to H1025 (550°C, 4 hours), the specimens achieved a nobler E_{Pit} (from 0.173 V to 0.205 V). However, Shoushtari [57] followed up that on even higher conditions of the H1150 (620°C, 4 hours), the localised corrosion resistance of the specimens would deteriorate, possibly due to the markedly different microstructure involving the coarsening of copper precipitates, leading to increased retained austenite [63], and lowering coherency of precipitates [63,66].

Pitting corrosion resistance depends on various factors, including heat treatment, chemical composition, and local environmental factors. In general, both the H1150 and H900 conditions improved the corrosion resistance of the EAM fabricated as-sinter samples. However, additional analysis of the microstructural differences is necessary for further insights into the specific corrosion mechanisms and differences between the two conditions, which is the avenue for future research.

Conclusions

This study provides valuable insights into the sinter-based additive manufacturing of 17-4 PH stainless steel, offering a holistic understanding of the intricate interplay between processing parameters, microstructural evolution, and material properties, particularly in the context of electrochemical corrosion resistance. The main conclusions are as follows

- Adequate interlayer adhesion was observed in the central region of as-printed samples, while defects were prominent near the edges. Sintering reduced porosity, increasing density from 62.3% to 95.1%, with isolated pores (2.6%) in the central region and higher porosities (5.1%–7.2%) near the edges. These defects led to variability in microhardness (66–347 HV).
- The as-sintered samples exhibited anisotropic mechanical behavior, with samples printed perpendicular to the build direction showing superior strength (28% higher σ_{UTS}) and ductility (eightfold increase in ε_f), whereas those printed along the build direction demonstrated better corrosion resistance, with nobler E_{corr} and E_{pit} values, suggesting that electrochemical characteristics of sinter-based AM fabricated components may differ from those of conventionally produced wrought parts.
- Machining of the as-sintered samples significantly improved tensile strength (12% increase in σ_{UTS}) and ductility (63% increase in ε_f), matching or surpassing values in BJ, EAM, and standards in MIM, and comparable to wrought and L-PBF counterparts.
- H900 heat treatment enhanced tensile properties, with 14% improvement in σ_{UTS} and 125% increase in ε_f, while H1150 led to a significant increase in ductility (203%) but a 19% reduction in σ_{UTS}. Pitting corrosion resistance improved with heat treatment, with H1150 showing the noblest E_{pit} (0.165 V), followed by H900 (0.107 V) and the as-sintered sample (-0.015 V).

Author Contributions

YanHan LIEW: Conceptualization, Validation, Visualization, Writing – Original Draft. **Aloysius TAN**: Methodology, Investigation, Writing – Original Draft. **Mojtaba SALEHI**: Conceptualization, Validation, Supervision, Writing – Review & Editing.

Conflicts of interest

There are no conflicts to declare.

Acknowledgements

The authors would like to acknowledge Mr. Christian Chandra, Dr. Sudesh Wijesinghe, Mr. Ong Wee Kit, and Mr. Gerard Ong for their contribution to the work.

References

1. Hunt J, Derguti F, Todd I. Selection of steels suitable for additive layer manufacturing. Ironmak Steelmak 2014;41(4):254–6.

2. Tavares SSM, da Silva FJ, Scandian C, da Silva GF, de Abreu HFG. Microstructure and intergranular corrosion resistance of UNS S17400 (17-4PH) stainless steel. Corros Sci [Internet] 2010;52(11):3835–9. Available from: http://dx.doi.org/10.1016/j.corsci.2010.07.016

3. Boswell B, Islam MN, Davies IJ, Ginting YR, Ong AK. A review identifying the effectiveness of minimum quantity lubrication (MQL) during conventional machining. Int J Adv Manuf Technol 2017;92(1–4):321–40.

4. Atzeni E, Salmi A. Economics of additive manufacturing for end-usable metal parts. Int J Adv Manuf Technol 2012;

5. Yin D, Gienger EB, Croom BP, Reider LA, Trethewey BR, Lark AR, et al. Variability in mechanical properties of additively manufactured 17-4 PH stainless steel produced by multiple vendors: insights for qualification. Int J Adv Manuf Technol [Internet] 2023;128(7–8):3093–103. Available from: https://doi.org/10.1007/s00170-023-12113-6

6. Drummond M, Eltaggaz A, Deiab I. 3D Printing of high melting iron alloys using metal-fused deposition modeling: a comprehensive review. Int J Adv Manuf Technol [Internet] 2023;(0123456789). Available from: https://doi.org/10.1007/s00170-023-12189-0

7. Quarto M. An empirical method for forecasting energy consumption in material extrusion. Int J Adv Manuf Technol [Internet] 2023;127(5–6):2911–20. Available from: https://doi.org/10.1007/s00170-023-11646-0

8. Armstrong M, Mehrabi H, Naveed N. An overview of modern metal additive manufacturing technology. J Manuf Process [Internet] 2022;84(October):1001–29. Available from: https://doi.org/10.1016/j.jmapro.2022.10.060

9. Tosto C, Tirillò J, Sarasini F, Sergi C, Cicala G. Fused Deposition Modeling Parameter Optimization for Cost-Effective Metal Part Printing. Polymers (Basel) 2022;14(16):1–22.

10. Gonzalez-Gutierrez J, Arbeiter F, Schlauf T, Kukla C, Holzer C. Tensile properties of sintered 17-4PH stainless steel fabricated by material extrusion additive manufacturing. Mater Lett [Internet] 2019;248:165–8. Available from: https://doi.org/10.1016/j.matlet.2019.04.024

11. Singh G, Missiaen JM, Bouvard D, Chaix JM. Additive manufacturing of 17–4 PH steel using metal injection molding feedstock: Analysis of 3D extrusion printing, debinding and sintering. Addit Manuf 2021;47:102287.

12. Pellegrini A, Guerra MG, Lavecchia F. Shrinkage evaluation and geometric accuracy assessment on 17–4 PH samples made by material extrusion additive manufacturing. J Manuf Process [Internet] 2024;109(May 2023):394–406. Available from: https://doi.org/10.1016/j.jmapro.2023.12.031

13. Pellegrini A, Lavecchia F, Guerra MG, Galantucci LM. Influence of aging treatments on 17–4 PH stainless steel parts realized using material extrusion additive manufacturing technologies. Int J Adv Manuf Technol [Internet] 2023 [cited 2024 Apr 29];126(1–2):163–78. Available from: https://link.springer.com/article/10.1007/s00170-023-11136-3

14. Pompeo V Di, Santecchia E, Santoni A, Spigarelli S, Sleem K, Cabibbo M. Microstructure and Defect Analysis of 17-4PH Stainless Steel Manufacturing Technology. 2023;

15. Cho YH, Park SY, Kim JY, Lee KA. 17-4PH stainless steel with excellent strength–elongation combination developed via material extrusion additive manufacturing. J Mater Res Technol [Internet] 2023;24:3284–99. Available from: https://doi.org/10.1016/j.jmrt.2023.03.228

16. Opoz TT, Burgess A, Ahuir-Torres JI, Kotadia HR, Tammas-Williams S. The effect of surface finish and post-processing on mechanical properties of 17-4 PH stainless steel produced by the atomic diffusion additive manufacturing process (ADAM). Int J Adv Manuf Technol [Internet] 2024;130(7–8):4053–66. Available from: https://doi.org/10.1007/s00170-024-12949-6

17. Sun X, Mazur M, Cheng CT. A review of void reduction strategies in material extrusion-based additive manufacturing. Addit Manuf [Internet] 2023;67(November 2022):103463. Available from: https://doi.org/10.1016/j.addma.2023.103463

18. Mancia T, Forcellese P, Bellezze T, Simoncini M. Effect of build-up orientation angle and printing speed on mechanical properties and micro- and macro-defect formation in 17-4 PH stainless steel components manufactured by Bound Metal Deposition. Int J Adv Manuf Technol [Internet] 2024;(0123456789). Available from: https://doi.org/10.1007/s00170-024-13628-2

19. Markforged. Material Datasheet 17-4 PH Stainless Steel. 2020;1–2.

20. ASTM International. ATSM A564/A564M-19a: Standard Specification for Hot-Rolled and Cold-Finished Age-Hardening Stainless Steel Bars and Shapes. 2019;

21. ASTM International. ASTM B962: Standard Test Methods for Density of Compacted or Sintered Powder Metallurgy (PM) Products Using Archimedes' Principle. Astm B962-13 2013;i:1–7.

22. ASTM International. ASTM E8/E8M-22: Standard Test Methods for Tension Testing of Metallic Materials. 2022;

23. Ryan MP, Williams DE, Chater RJ, Hutton BM, McPhail DS. Why stainless steel corrodes. Nature 2002;415(6873):770–4.

24. Raghavan V, Antia DP. The chromium equivalents of ferrite stabilizers in commercial stainless steels. Metall Mater Trans A 1994;25(12):2827–8.

25. Jones J, Vafadar A, Hashemi R. A Review of the Mechanical Properties of 17-4PH Stainless Steel Produced by Bound Powder Extrusion. 2023;

26. de Terris T, Andreau O, Peyre P, Adamski F, Koutiri I, Gorny C, et al. Optimization and comparison of porosity rate measurement methods of Selective Laser Melted metallic parts. Addit Manuf [Internet] 2019;28(May):802–13. Available from: https://doi.org/10.1016/j.addma.2019.05.035

27. AK Steel. 17-4 PH Stainless Steel.

28. Huber D, Vogel L, Fischer A. The effects of sintering temperature and hold time on densification, mechanical properties and microstructural characteristics of binder jet 3D printed 17-4 PH stainless steel. Addit Manuf [Internet] 2021;46(October 2020):102114. Available from: https://doi.org/10.1016/j.addma.2021.102114

29. Zhang Y, Roch A. Fused filament fabrication and sintering of 17-4PH stainless steel. Manuf Lett [Internet] 2022;33:29–32. Available from: https://doi.org/10.1016/j.mfglet.2022.06.004

30. Abe Y, Kurose T, Santos MVA, Kanaya Y, Ishigami A, Tanaka S, et al. Effect of layer directions on internal structures and tensile properties of 17-4ph stainless steel parts fabricated by

fused deposition of metals. Materials (Basel) 2021;14(2):1–12.

31. Suwanpreecha C, Seensattayawong P, Vadhanakovint V, Manonukul A. Influence of Specimen Layout on 17-4PH (AISI 630) Alloys Fabricated by Low-Cost Additive Manufacturing. Metall Mater Trans A Phys Metall Mater Sci [Internet] 2021;52(5):1999–2009. Available from: https://doi.org/10.1007/s11661-021-06211-x

32. Metal Powder Industries Federation. MPIF Standard 35 - Materials Standards for Metal Injection Molded Parts. 2022;

33. ASTM International. ASTM B883-19: Standard Specification for Metal Injection Molded (MIM) Materials. 2019;

34. Wu MW, Huang ZK, Tseng CF, Hwang KS. Microstructures, mechanical properties, and fracture behaviors of metal-injection molded 17-4PH stainless steel. Met Mater Int 2015;21(3):531–7.

35. Mukund BN, Hausnerova B. Variation in particle size fraction to optimize metal injection molding of water atomized 17–4PH stainless steel feedstocks. Powder Technol [Internet] 2020;368:130–6. Available from: https://doi.org/10.1016/j.powtec.2020.04.058

36. Narasimharaju SR, Zeng W, See TL, Zhu Z, Scott P, Jiang X, et al. A comprehensive review on laser powder bed fusion of steels: Processing, microstructure, defects and control methods, mechanical properties, current challenges and future trends. J Manuf Process [Internet] 2022;75(January 2021):375–414. Available from: https://doi.org/10.1016/j.jmapro.2021.12.033

37. LeBrun T, Nakamoto T, Horikawa K, Kobayashi H. Effect of retained austenite on subsequent thermal processing and resultant mechanical properties of selective laser melted 17–4 PH stainless steel. Mater Des [Internet] 2015;81:44–53. Available from: https://linkinghub.elsevier.com/retrieve/pii/S0261306915002721

38. Kumar SP, Babu PD. Effect of laser energy density on surface morphology, microstructure and mechanical behaviour of direct metal laser melted 17-4 PH stainless steel. Int J Mater Res 2023;114(10–11):911–24.

39. Giganto S, Martínez-Pellitero S, Barreiro J, Zapico P. Influence of 17-4 PH stainless steel powder recycling on properties of SLM additive manufactured parts. J Mater Res Technol 2022;16:1647–58.

40. Markforged. Material Datasheet 17-4 PH Stainless Steel v2. 2022;

41. Desktop Metal. 17-4PH Stainless Steel for Studio System^{TM} 2. 2021;1.

42. Galati M, Minetola P. Analysis of density, roughness, and accuracy of the atomic diffusion additive manufacturing (ADAM) process for metal parts. Materials (Basel) 2019;12(24).

43. Desktop Metal. 17-4PH Stainless Steel for Shop System^{TM}. 2020;1.

44. Tillmann W, Lopes Dias NF, Stangier D, Schaak C, Höges S. Heat treatment of binder jet printed 17–4 PH stainless steel for subsequent deposition of tribo-functional diamond-like carbon coatings. Mater Des [Internet] 2022;213:110304. Available from: https://doi.org/10.1016/j.matdes.2021.110304

45. Desktop Metal. 17-4PH Stainless Steel for Production System^{TM} P-1 or P-50. 2021;1.

46. Watson A, Belding J, Ellis BD. Characterization of 17-4 PH Processed via Bound Metal Deposition (BMD). Miner. Met. Mater. Ser.2020;205–16.

47. German R. Sintering: From Empirical Observations to Scientific Principles [Internet]. Elsevier Inc.; 2014 [cited 2024 Mar 14]. Available from: http://www.sciencedirect.com:5070/book/9780124016828/sintering-from-empirical-observations-to-scientific-principles

48. Alfieri V, Giannella V, Caiazzo F, Sepe R. Influence of position and building orientation on the static properties of LPBF specimens in 17-4 PH stainless steel. Forces Mech [Internet] 2022;8(May):100108. Available from: https://doi.org/10.1016/j.finmec.2022.100108

49. Yadollahi A, Mahmoudi M, Elwany A, Doude H, Bian L, Newman JC. Effects of crack orientation and heat treatment on fatigue-crack-growth behavior of AM 17-4 PH stainless steel. Eng Fract Mech [Internet] 2020;226(October 2019):106874. Available from: https://doi.org/10.1016/j.engfracmech.2020.106874

50. Mahmoudi M, Elwany A, Yadollahi A, Thompson SM, Bian L, Shamsaei N. Mechanical properties and microstructural characterization of selective laser melted 17-4 PH stainless steel. Rapid Prototyp J 2017;23(2):280–94.

51. S PK, P DB, Gautam J, Rai AK, Paul CP. Synergistic integration of laser shock peening and heat treatment for refined microstructure and enhanced mechanical properties in additively manufactured 17–4PH stainless steel. J Mater Process Technol [Internet] 2024;328(December 2023):118395. Available from: https://doi.org/10.1016/j.jmatprotec.2024.118395

52. Basalah A, Shanjani Y, Esmaeili S, Toyserkani E. Characterizations of additive manufactured porous titanium implants. J Biomed Mater Res - Part B Appl Biomater [Internet] 2012 [cited 2024 Mar 14];100 B(7):1970–9. Available from: https://onlinelibrary-wiley-com.ejproxy.a-star.edu.sg/doi/full/10.1002/jbm.b.32764

53. Salehi M, Kuah KX, Huang Z, Blackwood DJ, Zhang SX, Seet HL, et al. Enhancing densification in binder jet additive manufacturing of magnesium via nanoparticles as sintering aids. J Manuf Process 2023;99:705–17.

54. Schaller RF, Taylor JM, Rodelas J, Mishra A, Schindelholz EJ. Corrosion properties of powder bed fusion additively manufactured stainless steels. Mater Sci Technol Conf Exhib 2017, MS T 2017 2017;2(July):1083–5.

55. Forcellese P, Mancia T, Simoncini M, Bellezze T. Investigation on Corrosion Resistance Properties of 17-4 PH Bound Metal Deposition As-Sintered Specimens with Different Build-Up Orientations. Metals (Basel) 2022;12(4).

56. Kazior J. Influence of Sintering Atmosphere, Temperature and the Solution-Annealing Treatment on the Properties of Precipitation-Hardening Sintered 17-4 PH Stainless Steel. Materials (Basel) 2023;16(2).

57. Shoushtari MRT. Effect of ageing heat treatment on corrosion behavior of 17-4 PH stainless steel in 3 . 5 % NaCl. Int J ISSI 2010;7(1):33–6.

58. Szewczyk-Nykiel A, Kazior J. Effect of Aging Temperature on Corrosion Behavior of Sintered 17-4 PH Stainless Steel in Dilute Sulfuric Acid Solution. J Mater Eng Perform 2017;26(7):3450–6.

59. Williams DE, Zhu YY. Explanation for Initiation of Pitting Corrosion of Stainless Steels at Sulfide Inclusions. J Electrochem Soc 2000;147(5):1763.

60. Ko G, Kim W, Kwon K, Lee TK. The corrosion of stainless steel made by additive manufacturing: A review. Metals (Basel) 2021;11(3):1–21.

61. Esmailzadeh S, Aliofkhazraei M, Sarlak H. Interpretation of Cyclic Potentiodynamic Polarization Test Results for Study of Corrosion Behavior of Metals: A Review. Prot Met Phys Chem Surfaces 2018;54(5):976–89.

62. Stoudt MR, Ricker RE, Lass EA, Levine LE. Influence of Postbuild Microstructure on the Electrochemical Behavior of Additively Manufactured 17-4 PH Stainless Steel. Jom 2017;69(3):506–15.

63. C.N. Hsiao, C.S. Chiou, J.R. Yang. Aging reactions in a 17-4 PH stainless steel. Mater Chem Phys 2002;74(2):134–42.

64. ExOne. 17-4PH Stainless Steel for X-Series. 2020;1.

65. Radhakrishnan J, Kumar P, Gan SS, Bryl A, McKinnell J, Ramamurty U. Microstructure and tensile properties of binder jet printed 17–4 precipitation hardened martensitic stainless steel. Mater Sci Eng A 2022;860:144270.

66. Habibi Bajguirani HR. The effect of ageing upon the microstructure and mechanical properties of type 15-5 PH stainless steel. Mater Sci Eng A 2002;338(1–2):142–59.